



HHS Public Access

Author manuscript

Acad Radiol. Author manuscript; available in PMC 2017 October 25.

Published in final edited form as:

Acad Radiol. 2016 April ; 23(4): 457–467. doi:10.1016/j.acra.2015.12.015.

Rapid High-resolution, Self-registered, Dual Lumen-contrast MRI Method for Vessel-wall Assessment in Peripheral Artery Disease: A Preliminary Investigation

Michael C. Langham, PhD,

Departments of Radiology, University of Pennsylvania School of Medicine, 3400 Spruce St. 19104, Philadelphia, PA

Benoit Desjardins, MD, PhD,

Departments of Radiology, University of Pennsylvania School of Medicine, 3400 Spruce St. 19104, Philadelphia, PA

Erin K. Englund, BE,

Departments of Radiology, University of Pennsylvania School of Medicine, 3400 Spruce St. 19104, Philadelphia, PA

Emile R. Mohler III, MD,

Department of Medicine, University of Pennsylvania School of Medicine, Philadelphia, Pennsylvania

Thomas F. Floyd, MD, and

Departments of Anesthesiology, Stony Brook University Medical Center, Stony Brook, New York

Felix W. Wehrli, PhD

Departments of Radiology, University of Pennsylvania School of Medicine, 3400 Spruce St. 19104, Philadelphia, PA

Abstract

Rationale and Objectives—Contrast-enhanced angiographic evaluation by magnetic resonance imaging (MRI) and computed tomography (CT) is the reference standard for assessing peripheral artery disease (PAD). However, because PAD and diabetes often coexist, the prevalence of renal insufficiency is a major challenge to contrast-based angiography. The objective of this work is to describe and demonstrate a new application of three-dimensional double-echo steady-state (3D DESS) as a noncontrast vascular MRI method for evaluating peripheral atherosclerosis at 3 Tesla (3T).

Materials and Methods—A water-selective 3D DESS pulse sequence was designed to simultaneously collect two steady-state free-precession signals (free induction decay and Echo) yielding “black blood” (BB) and “gray blood” (GB) images. For completeness Bloch equation, simulations were performed to characterize DESS signals of various tissues including blood at different velocities and to assess two healthy subjects for the purpose of pulse sequence optimization. Exploratory studies were performed as an add-on protocol to an existing study

Address correspondence to: F.W.W. wehrli@mail.med.upenn.edu.

involving patients with PAD. To evaluate the method's specificity for detecting calcification, images from select patients were compared against CT angiography.

Results—Simulations agreed qualitatively with *in vivo* images supporting DESS' potential for generating distinct lumen contrast (GB vs BB). Lesions representing calcium were easily identifiable on the basis of signal void occurring on both image types and were confirmed by CT angiography. Further, BB allowed visualization of stent restenosis, and data suggest its ability to visualize acute thrombus by virtue of T2 weighting.

Conclusion—Preliminary investigation and results suggest noncontrast 3D DESS to have the potential to improve diagnosis of PAD patients by providing detailed structural assessment of vessel-wall architecture.

Keywords

Black-blood imaging; gray-blood imaging; vessel-wall imaging; calcification; double-echo steady-state; peripheral artery disease; SSFP-FID; SSFP-Echo; angiography

INTRODUCTION

Peripheral artery disease (PAD) is a common manifestation of systemic atherosclerosis affecting 8–12 million individuals in the United States. Patients with PAD have a fivefold and a two- to threefold greater risk of heart attack and stroke, respectively, and higher mortality rate relative to those without PAD (1). Among subjects aged 50 years and older with diabetes mellitus and a history of smoking, the prevalence of PAD can be as high as 30% (2). The most common clinical symptom is intermittent claudication or cramp-like pain in the legs and buttocks induced by exercise, which contributes to a poor quality of life and a high rate of depression (3,4). The progression of the disease can lead to critical limb ischemia where blood flow is severely impaired to the lower limbs due to stenosis.

Maximum intensity projections of contrast-based angiography can rapidly provide a “roadmap” of large vascular segments for the assessment of severity and extent of PAD. Typical spatial resolution of contrast-enhanced magnetic resonance angiography (CE-MRA) is limited to 1 mm, and the luminal images cannot provide tissue information such as vessel-wall thickening and calcification. Computed tomographic angiography (CTA) is often preferred for speed and high-isotropic resolution, allowing reformation in any direction. However, diffuse calcification can confound diagnosis, particularly in smaller infrapopliteal arteries, which are common sites of PAD in diabetics (5,6). The gold standard for evaluating vascular diseases is catheter-based digital subtraction angiography (DSA), often utilized for planning surgical revascularization and angioplasty. Both CTA and DSA expose patients to ionization radiation. The greatest challenge of contrast-based angiography occurs in patients with compromised renal function, where prevalence is estimated at 27–36% (7) because PAD and diabetes often coexist (8). Paradoxically, this is the patient population most indicated for angiographic examination, but these patients have a greater risk of contrast-induced acute renal failure, a source of significant morbidity and mortality.

One of the most promising noncontrast or unenhanced MRA techniques is nonsubtractive, cardiac-gated, “quiescent interval single-shot” (QISS) (9). Unlike the conventional time-of-

flight (TOF) MRA (10), full inflow refreshment is achieved for each slice even at flow velocities as low as 1 cm/s due to the long quiescent interval (~230 ms). At 1.5T QISS compared favorably with both CE-MRA and DSA in terms of identifying significant stenoses (11). However, at 3T B_1 inhomogeneity leads to signal loss in the proximal right femoral artery as a result of symmetric B_1 field minima on the anterior medial side of the right leg and the posterior medial side of the left leg (12). Further, the signal loss in the presence of a stent results in nondiagnostic images precluding assessment of stent patency (9).

Angiography, which is based on luminal imaging techniques, do not provide information on arterial wall remodeling, or distinguish plaque from focal arterial thrombus. Further, diffuse calcification can confound X-ray-based arteriograms in smaller runoff arteries. The detection of calcification is important for the planning of intervention to avoid adverse events, which include severe dissections, vessel perforations, and atheroembolization (13). In the presence of heavy calcification, the results of balloon angioplasty are often suboptimal (14). The limitations mentioned can be overcome with spatially registered gray-blood (GB) and black-blood (BB) images (15). The calcification will appear as signal void on GB and BB images due to submillisecond T_2 (16). However, on GB images, the lumen signal intensity will be moderate, therefore, calcium can be identified readily by inspecting GB and BB images together (15). Lastly, better visualization of plaque morphology from BB images provides more accurate estimation of stenosis severity.

In this work, we present a simple approach to simultaneously acquire spatially registered GB and BB images for evaluating plaque burden, which entails visualization of vessel-wall remodeling and identification of calcium and focal arterial thrombus in patients with PAD, using a water-selective three-dimensional double-echo steady-state (3D DESS) pulse sequence. Previously, DESS has been applied for structural (17) and diffusion-weighted (18) imaging of knee cartilage. DESS collects two unbalanced steady-state free precession (SSFP) signals, commonly known as SSFP-free induction decay (FID) and SSFP-Echo (19), which are inherently flow sensitive because steady state cannot be attained for spins moving along a magnetic field gradient. The simultaneous acquisition of GB and BB images achieves automatic spatial registration and reduction in acquisition time by almost 50%. Here, the difference in the flow sensitivity of FID and Echo is evaluated with Bloch equation simulations of the DESS signal with and without bulk flow. Further, a new application of the 3D DESS sequence is demonstrated on both healthy subjects and selected patients with PAD.

METHODS

Blood Signal Attenuation in 3D DESS

The 3D DESS, which collects SSFP-FID and SSFP-Echo signals used in this work, is shown in Figure 1. Fat attenuation is achieved with a 1–1 binomial pulse so as to restore the magnetization of the fat CH_2 protons along the z axis, which requires the 2nd radio frequency (RF) pulse to be applied after one half-period of the fat–water chemical shift difference at 3T. The structure of the pulse sequence is identical to the implementation in Bieri et al (18) except that a unipolar crusher gradient pulse is applied along the slice

direction (craniocaudal) to achieve maximum flow sensitivity while minimizing muscle tissue signal loss via diffusion. Also, the absence of rephase and prephase lobes for the FID and Echo readout, respectively, leads to flow sensitivity in the readout direction (left to right) as well; with net zeroth gradient moment of $32.38 \text{ mT} \times \text{ms/m}$, sufficient to impart dephasing of 2π across 0.7 mm . The essential feature of the DESS sequence is the separation of FID and Echo (2nd readout) in k-space, achieved by dephasing of 4π (20) across the voxel along the slice-encoding direction. The Echo signal has some T_2^* weighting because the actual echo (partially refocused FID from the previous pulse cycle) occurs at repetition time ($2TR$). The FID was read out at larger bandwidth to minimize TR (at some loss of signal-to-noise ratio [SNR], of course), thereby optimizing the Echo signal and minimizing chemical shift artifact, as the water selectivity of the 1–1 binomial pulse is somewhat less effective for the FID (See Results section).

The main contribution to the FID signal is the newly tipped transverse magnetization (no phase history) because the readout occurs before the application of the crusher gradient. In 2D imaging, the FID signal further benefits from inflow enhancement. However, in a large slab, 3D acquisition with $TR \ll T_2$ the spins of blood water will experience many RF pulses before exiting the slab, therefore causing signal attenuation from saturation. Also, the number of magnetization components will grow rapidly as every RF pulse splits each component into three. Further, the phases of the components accumulate quadratically in pulse cycle number n in the presence of the unbalanced crusher gradient along the flow

direction, $\phi_n = \frac{1}{2}\phi_o(n^2 + n + 2)$. The phase increment $\phi_o = \gamma m_o v_o TR$, where γ is the gyromagnetic ratio of proton, m_o is the zeroth moment of the unbalanced gradient, v_o is the flow speed of the proton along the magnetic field gradient and TR is the repetition time. The superposition of these components tends to be destructive, thereby significantly attenuating the blood signal (21). The SSFP-Echo signal, also formed from superposition of numerous magnetization components generated from each RF pulse, is lower than the FID signal because the primary signal is the partially refocused FID from the previous pulse cycle. The refocused signal is further reduced for the spins that move along the direction of the unbalanced gradient whose effect is equivalent to motion sensitizing (bipolar gradients) separated by TR .

Numerical Simulation

Bloch equation simulations were first performed to determine the optimum flip angle of the DESS sequence to optimize the SSFP-Echo signal of muscle tissue for $T_1/T_2/TR = 1450/30/10.6 \text{ ms}$. The flow sensitivity of FID and Echo was evaluated for a range of constant velocities ($0.1\text{--}10 \text{ cm/s}$), as well as the performance of fat attenuation with the 1–1 binomial pulse in the presence of static field inhomogeneity. In the simulations, it was assumed that the spins are within the slab at all times from the initial magnetization $M_{z,o} = 1$, and $T_2/T_1 = 200/1700 \text{ ms}$ and $100/400 \text{ ms}$ were used for arterial blood and subcutaneous fat (chemical shift at -418 Hz), respectively. The inflow enhancement at the proximal edge can be assessed based on the number of pulse cycles required to achieve steady-state blood signal.

In Vivo Study

3D *in vivo* images of the femoropopliteal and infra-popliteal arteries of two young healthy volunteers (average age 29 years) were acquired with the 3D DESS pulse sequence of Figure 1 using the spine and two body matrix coils or spine with peripheral arteries (PA) matrix coils at 3T (Siemens TIM Trio). In healthy young controls, patent arterial lumina are expected, allowing evaluation of 3D DESS images for stenosis-mimicking artifacts and for effectiveness of blood suppression as well as attenuation of fat signal; two subjects suffice for this purpose. To evaluate 3D DESS for visualizing a wide range of lesion and calcium severity, images of femoropopliteal arteries were acquired on 20 patients with PAD as an add-on protocol to an existing study (22). One of the patients with diffuse calcification underwent CTA 3 months after the magnetic resonance imaging (MRI) study, and in five patients, there was enough time to perform QISS MRA. Both water-selective 3D DESS and QISS were implemented in SequenceTree (23). In five patients, infra-popliteal arteries were imaged to assess visualization of smaller runoff arteries and to show that the proposed method is not confounded by diffuse calcification. Femoropopliteal arteries were imaged with the following parameters: flip angle $8^\circ + 8^\circ$, $TE_{\text{FID}}/TE_{\text{echo}}/TR = 2.2/7.8/10.6$ ms, bandwidth = 744 Hz/voxel (FID), 223 Hz/voxel (Echo), field-of-view (FOV) = $352 \times 192 \times 360$ mm³, spatial resolution = $0.78 \times 0.78 \times 3$ mm³, NEX = 1, acquisition time (TA) = 5.2 min. Smaller FOV and higher spatial resolution were used for infrapopliteal arteries, FOV = $288 \times 128 \times 360$ mm³, spatial resolution = $0.64 \times 0.64 \times 3$ mm³ (TA = 4.4 min) but the remaining parameters were kept the same. Images were zero padded to $0.39 \times 0.39 \times 1.5$ mm³ or $0.32 \times 0.32 \times 1.5$ mm³. Imaging parameters of QISS MRA: FOV 320×192 mm², 5/8 partial Fourier centric acquisition, spatial resolution 1 mm², slice thickness 4 mm with 1 mm overlap (65 slices/station), trigger delay 100 ms, quiescent interval 180 ms, TE/TR = 2.05/4.1 ms and flip angle was limited to 50° – 82° due to specific absorption rate (SAR). Written informed consent was obtained before all examinations following an institutional review board-approved protocol.

SNR, CNR, and Fat Attenuation Level

For each patient the vessel-wall and lumen SNR of common femoral, superficial femoral, and popliteal arteries in right leg were computed to assess reliability of the method. SNR was computed as SI/σ , where SI is the signal intensity of the ROI, and σ is the standard deviation of noise, determined from a region in the air surrounding the legs (24). contrast-to-noise ratio (CNR) between the vessel-wall and lumen was defined as the SNR difference between two adjacent structures. The percent reduction in fat signal by the binomial 1–1 excitation pulse (2_{RF}) was defined with respect to images acquired with single excitation RF pulse (1_{RF}), i.e. as $100 \times |1_{\text{RF}} - 2_{\text{RF}}|/1_{\text{RF}}$.

RESULTS

Numerical Simulations

Bloch equation simulations of FID and Echo for a range of velocities and resonance offsets are shown in Figure 2. The steady-state signals of FID and Echo are predicted to be comparable for stationary blood because $T_2 \gg TR$. On the other hand, the Echo is attenuated significantly more than the FID (95% vs 64%) for spins moving with average

velocity 0.5 cm/s. For reference, muscle tissue signal is also plotted. From Figure 2a we can conclude that once the spins enter the excited slab, the inflow enhancement for the FID signal decreases rapidly with the number of pulse sequence cycles (except at very low velocities). For average velocities of 5 cm/s hyperintense, lumen signal is expected on FID images near the proximal edge of the slab, gradually decreasing toward a steady-state signal level at about 50 mm. In Figure 2c, FID and Echo signal of fat as a function of resonance offset are plotted and the FID signal of muscle tissue is included for reference. On resonance (0 Hz), the lipid CH₂ protons will precess by 180° during the interpulse time (1.196 ms), whereas at +200 Hz, the precession angle is approximately 90°, which translates to lower effective flip angle of 0 and 8°, respectively. The muscle tissue signal is less affected by off-resonance. According to Bloch equation simulation (not shown), muscle tissue FID signal does not vary appreciably (<3%) for flip angles between 8° and 16° but the Echo signal will be reduced by as much as 20%.

In Vivo Study

Representative axial SSFP-FID (GB) and SSFP-Echo (BB) images of a healthy 30-year-old subject are shown in Figure 3. Distal to the proximal edge of the 3D slab, the blood or the lumen signal in the GB image (Fig 3a) is attenuated below the signal level of muscle tissue as predicted by the simulation (Fig 2a). The vessel-wall and lumen SNR of common femoral, superficial femoral, and popliteal arteries are summarized in Tables 1 and 2 for BB and GB images, respectively. The average vessel-wall and lumen SNR across all patients and vessels were 36.5 ± 16.7 and 35.3 ± 13.4 on GB images, and 26.0 ± 8.2 and 8.3 ± 2.2 on BB images, which translates to average CNR between vessel-wall and lumen of 2.6 and 17.7 for GB and BB images. The trend of decreased average lumen SNR in GB images from common femoral to popliteal arteries reflects proximal inflow enhancement and subsequent signal attenuation distally as the blood water protons experience more RF pulses. On BB images, the reliability of blood signal suppression is indicated by the lower standard deviation of lumen SNR compared to other SNR measurements.

Like other fat suppression techniques, the effectiveness of binomial pulse is sensitive to magnetic field inhomogeneity. As predicted by simulation (Fig 2c), the subcutaneous and intermuscular fat signal was attenuated less by the 1–1 binomial pulse on GB (Fig 3a) compared to BB images (Fig 3b) because the former, being a gradient-echo and having much shorter TE, is more sensitive to field inhomogeneity. As a result of field inhomogeneity, the adipose signal intensity varied somewhat across the FOV (circles on Fig 3a). For comparison GB and BB images without fat attenuation are shown in Figure 3c and d, i.e. single versus dual RF excitation with the same net flip angle. The average reduction of the adipose signal for binomial 1–1 pulse were excitation 65% and 85% on GB and BB images, respectively, relative to single RF excitation. The inflow blood signal enhancement can be seen in the magnified view of the femoral artery in the GB image (Fig 3e), whereas the blood signal is largely suppressed with vessel walls well delineated in the BB image (Fig 3f) from proximal to distal edge of the 3D slab. The inflow enhancement of the BB image agrees qualitatively with Figure 2a because the slices in Figure 3e are separated by 45 mm.

Figure 4a and b (Subject 9) shows correlative GB and BB images of the iliac arteries from a patient with PAD demonstrating calcification (white arrow), which is corroborated by the arterial phase CTA (Fig 4c). On the CTA image patent lumen and calcium are hyperintense relative to surrounding tissue. The distinction of patent lumen from calcium relies on the higher CT density of calcium compared to contrast material. On the GB images, the detection of calcium is apparent by signal voids adjacent to lumen (Fig 4a), further demonstrated in Figure 5 (Subject 2), where calcium is readily identified on GB image (Fig 5a), again confirmed by CTA (Fig 5b). Albeit smaller, in tibial-peroneal trunk vessels, diffuse calcium can still confound CTA, corresponding signal loss is clearly visible on GB images (Fig 5c). Further, spatially registered GB (Fig 5d) and BB (Fig 5e) images allow the detection of calcium- and plaque-obstructing blood flow, which shows up hypointense on CTA (Fig 5f) due to the absence of contrast material.

Figure 6a (Subject 15) illustrates the complementary information high-resolution BB images provided relative to angiography (Fig 6b), including details of vessel-wall remodeling (blue dashed arrow in a) and lesion eccentricity (e.g. blue solid arrow), which are invisible on MRA (Fig 6b). From Figure 6a, the BB images by themselves are also well suited for visualizing lesion burden associated with PAD. The achievable spatial resolution of BB image is expected to yield higher confidence and more accurate lesion sizing. In general, DESS is less susceptible to artifactual signal loss at 3T from B1 inhomogeneity (25) in the proximal right femoral artery (see Fig 6 caption) compared to bSSFP. However, the issue of B1 inhomogeneity can be minimized with placement of a high-permittivity pad (25,26).

A significant limitation of MRA (particularly noncontrast) is the signal loss in the presence of a stent that can result in nondiagnostic images as illustrated in Figure 7a (maximum intensity projection [MIP] of QISS MRA, Subject 4). The magnified views of BB images in Figure 7b shows evidence of in-stent restenosis. As in a patent lumen, intravascular signal void is expected for a patent stent on BB image while retaining moderate blood signal in GB image. In addition to stent-related artifact, it is difficult to visualize the right proximal superficial femoral arteries (SFA) on the MIP due to signal loss associated with B₁ inhomogeneity. Because angiography is based on vessel patency, focal arterial thrombi cannot be distinguished from negative vessel-wall remodeling. The detection of thrombi (a frequent clinical consequence of atherosclerosis) is notoriously problematic. According to Corti et al (27), acute thrombus will appear strongly hyperintense on T2-weighted images, reaching peak signal at 1 week upon formation, and decreasing thereafter to a plateau by 6 weeks, eventually becoming isointense with muscle. On T1-weighted image, the time-course of the signal intensity is similar but with lower signal compared to T2 weighting. Whereas the GB image has mixed weighting (T1 and T2), the BB image is strongly T₂ weighted. Based on these observations, it is plausible to conclude that the cause of hyperintensity in the SFA lumen shown on Figure 8a and b (Subject 8) is a recently formed thrombus, whereas the thrombus shown in Figure 8c is several weeks old.

DISCUSSION

In this preliminary investigation, a new potential application of 3D DESS has been presented, simultaneous acquisition of spatially registered images of distinct lumen contrast.

The gray- and black-blood images of 3D DESS enables assessment of arterial wall remodeling, lesion eccentricity, and detection of calcification along with the evidence of identifying focal arterial thrombus, which are essential information for the planning of percutaneous interventions. 3D DESS also has the potential to overcome a very important limitation of CTA in diabetic patients where extensive diffuse calcification (Fig 5c) in infrapopliteal arteries prevents assessment of lumen patency (28).

3D DESS is a rapid unbalanced SSFP pulse sequence that enables acquisition of large-FOV high-resolution images in clinically practical scan times. The entire lower body arterial vasculature comprising the iliac arteries down to foot (over 100 cm along craniocaudal direction) can be covered in less than 13 min, thus it is feasible to pair 3D DESS with rapid noncontrast MRA (e.g. QISS (9)) for improved structural assessment of the vasculature for improved diagnosis and treatment planning in PAD patients, particularly in the presence of stents.

Our work shows that 3D DESS can detect calcification over a large FOV without the need for a separate acquisition. The detection of calcification is critical for patient management and prognosis. The presence of calcification has been shown to be closely associated with prevalence and severity of PAD and to be a better predictor of critical limb ischemia in patients on hemodialysis (29). Additionally, in patients with type-2 diabetes, calcification coexists in coronary and lower limb arteries and has been established as an independent predictor of cardiovascular mortality (30). Although CT is widely regarded as gold standard for calcium detection, it exposes patient to potentially harmful ionizing radiation and, more importantly, contrast-enhanced CTA is contraindicated in patients with renal insufficiency, such as patients with diabetes (a significant segment of the PAD population).

Recently, a 3D BB MRI technique, motion-sensitized driven equilibrium rapid gradient-recalled echo (GRE) (denoted MERGE), had been modified for simultaneous acquisition of spatially registered GB and BB images as a means to visualize deep-seated and superficial calcified nodules in the carotid arteries (15). However, the method's application to PA of the lower limb to estimate plaque size and morphology of the plaque burden has been limited (31) and to date, dual contrast (GB and BB) with 3D MERGE has not been demonstrated in the peripheral vascular bed to authors' knowledge. An alternative MRI approach for detecting calcification was proposed by Edelman et al (32), using thick-slab projection images of high-resolution (1 mm³) 3D GRE and prototype version of point-wise encoding time reduction with radial acquisition (33) at 1.5T. The focus of that work was on visualization of calcification via thick-slab projection and displaying the images inverted to generate CT-like images for assessing calcium burden over a large FOV. However, Edelman et al's technique does not yield BB images, whereas the detection of calcium is just one feature of our approach, which is a general method for plaque detection, visualization of vessel-wall remodeling and potentially, identification recently formed thrombus based on T2 weighting.

3D DESS is a robust and an SNR-efficient pulse sequence. Although projection images cannot be generated from the GB and BB images (which obviates the need to inspect source images), this should not be a serious limitation as we envision 3D DESS as an alternative

approach for evaluating plaque burden in PAD and not solely for calcium detection. We note in passing that angiographic source images are generally read slice by slice as a means to confirm findings on MIPs and to better estimate the degree of stenosis.

Among the method's limitation is that 3D DESS cannot provide comprehensive assessment of plaque composition because the BB image of SSFP-Echo is T₂ weighted, i.e. additional T₁ and proton density-weighted images would be needed (34,35). In PA, structural imaging has been limited to studies assessing arterial remodeling (36,37), whereas identification of vulnerable plaques and assessment of their composition has been largely confined to carotid and coronary arteries (see for example References 38 and 39). Although vulnerable plaques were investigated in patients with PAD, coverage was limited to a segment of less than 3 cm of the SFA (40) because the acquisition of multicontrast images is challenging given the large number of images needed to cover the entire vascular territory of the leg; the same holds true for alternative approaches. Nevertheless, recent studies using intravascular ultrasound (US) (41) suggest that the identification of vulnerable plaques or plaque ruptures in PA is potentially important in terms of patient management and prognosis. Okura et al found that there was a significant association between plaque rupture in iliofemoral arteries in patients with severe PAD and high prevalence of history of acute coronary syndrome.

As stated earlier, SSFP-Echo is extremely sensitive to flow, thus significant signal attenuation of slow-moving spins is easily achieved. For this reason, 3D DESS is less suited for arterial segments that are known to be more affected by motion such as carotid arteries from swallowing and coronary or central arteries from the cardiac motion. In contrast, in the PA patient motion is minimal, and the immobilization of the leg can further minimize movement artifacts and, as our data show, the acquisition of diagnostic-quality images of the iliac arteries with SSFP-Echo is straightforward (see Fig 4b).

CONCLUSION

We have described a new application of 3D DESS for simultaneously acquiring dual-contrast images to visualize lesion severity and luminal geometry, to assess arterial wall remodeling, and to identify calcium and newly formed thrombus in PA. 3D DESS is a rapid pulse sequence available on many commercial scanners and can be performed alone or in combination with an unenhanced MRA protocol requiring minimal patient setup and discomfort (e.g. no requirement for cardiac gating, nephrotoxic contrast agents, and ionizing radiation) for overall improved diagnosis and management of PAD.

Acknowledgments

This work was supported by NIH Grants K25 HL111422, R01 HL075649, R01 HL109545, and EE received support from AHA pre-doctoral fellowship.

References

1. Criqui MH, Langer RD, Fronek A, et al. Mortality over a period of 10 years in patients with peripheral arterial disease. *N Engl J Med.* 1992; 326:381–386. [PubMed: 1729621]
2. Hirsch AT, Haskal ZJ, Hertzner NR, et al. ACC/AHA 2005 Practice Guidelines for the management of patients with peripheral arterial disease (lower extremity, renal, mesenteric, and abdominal

aortic): a collaborative report from the American Association for Vascular Surgery/Society for Vascular Surgery, Society for Cardiovascular Angiography and Interventions, Society for Vascular Medicine and Biology, Society of Interventional Radiology, and the ACC/AHA Task Force on Practice Guidelines (Writing Committee to Develop Guidelines for the Management of Patients with Peripheral Arterial Disease): endorsed by the American Association of Cardiovascular and Pulmonary Rehabilitation; National Heart, Lung, and Blood Institute; Society for Vascular Nursing; TransAtlantic Intersociety Consensus; and Vascular Disease Foundation. *Circulation*. 2006; 113:e463–e654. [PubMed: 16549646]

3. McDermott MM, Greenland P, Guralnik JM, et al. Depressive symptoms and lower extremity functioning in men and women with peripheral arterial disease. *J Gen Intern Med*. 2003; 18:461–467. [PubMed: 12823653]
4. Regensteiner JG, Hiatt WR, Coll JR, et al. The impact of peripheral arterial disease on health-related quality of life in the peripheral arterial disease awareness, risk, and treatment: new resources for survival (PARTNERS) Program. *Vasc Med*. 2008; 13:15–24. [PubMed: 18372434]
5. American Diabetes A. Peripheral arterial disease in people with diabetes. *Diabetes Care*. 2003; 26:3333–3341. [PubMed: 14633825]
6. Strandness DE Jr, Priest RE, Gibbons GE. Combined clinical and pathologic study of diabetic and nondiabetic peripheral arterial disease. *Diabetes*. 1964; 13:366–372. [PubMed: 14210680]
7. Paraskevas KI, Giannoukas AD, Mikhailidis DP. Renal function impairment in peripheral arterial disease: an important parameter that should not be neglected. *Ann Vasc Surg*. 2009; 23:690–699. [PubMed: 19747617]
8. Murabito JM, D'Agostino RB, Silbershatz H, et al. Intermittent claudication. a risk profile from the framingham heart study. *Circulation*. 1997; 96:44–49. [PubMed: 9236415]
9. Edelman RR, Sheehan JJ, Dunkle E, et al. Quiescent-interval single-shot unenhanced magnetic resonance angiography of peripheral vascular disease: technical considerations and clinical feasibility. *Magn Reson Med*. 2010; 63:951–958. [PubMed: 20373396]
10. Meaney JF. Magnetic resonance angiography of the peripheral arteries: current status. *Eur Radiol*. 2003; 13:836–852. [PubMed: 12664125]
11. Hodnett PA, Ward EV, Davarpanah AH, et al. Peripheral arterial disease in a symptomatic diabetic population: prospective comparison of rapid unenhanced MR angiography (MRA) with contrast-enhanced MRA. *AJR Am J Roentgenol*. 2011; 197:1466–1473. [PubMed: 22109304]
12. Storey, P., Lee, VS., Sodickson, DK., et al. B1 inhomogeneity in the thigh at 3T and implications for peripheral vascular imaging. Hawaii: 2009.
13. Rocha-Singh KJ, Zeller T, Jaff MR. Peripheral arterial calcification: prevalence, mechanism, detection, and clinical implications. *Catheter Cardiovasc Interv*. 2014; 83:E212–E220. [PubMed: 24402839]
14. Schillinger M, Sabeti S, Loewe C, et al. Balloon angioplasty versus implantation of nitinol stents in the superficial femoral artery. *N Engl J Med*. 2006; 354:1879–1888. [PubMed: 16672699]
15. Koktzoglou I. Gray blood magnetic resonance for carotid wall imaging and visualization of deep-seated and superficial vascular calcifications. *Magn Reson Med*. 2013; 70:75–85. [PubMed: 22887594]
16. Du J, Corbeil J, Znamirovski R, et al. Direct imaging and quantification of carotid plaque calcification. *Magn Reson Med*. 2011; 65:1013–1020. [PubMed: 21413065]
17. Hardy PA, Recht MP, Piraino D, et al. Optimization of a dual echo in the steady state (DESS) free-precession sequence for imaging cartilage. *J Magn Reson Imaging*. 1996; 6:329–335. [PubMed: 9132098]
18. Bieri O, Ganter C, Scheffler K. Quantitative in vivo diffusion imaging of cartilage using double echo steady-state free precession. *Magn Reson Med*. 2012; 68:720–729. [PubMed: 22161749]
19. Bernstein, MA., King, KF., Zhou, JX. Handbook of MRI pulse sequences. Burlington, MA: Elsevier Academic Press; 2004. p. 589-592.
20. Hennig J. Multiecho imaging sequences with low refocusing flip angles. *J Magn Reson*. 1988; 78:397–407.
21. Zur Y, Wood ML, Neuringer LJ. Motion-insensitive, steady-state free precession imaging. *Magn Reson Med*. 1990; 16:444–459. [PubMed: 2077335]

22. Englund EK, Langham MC, Ratcliffe SJ, et al. Multiparametric assessment of vascular function in peripheral artery disease: dynamic measurement of skeletal muscle perfusion, blood-oxygen-level dependent signal, and venous oxygen saturation. *Circ Cardiovasc Imaging*. 2015; 8
23. Magland JF, Li C, Langham MC, et al. Pulse sequence programming in a dynamic visual environment: sequencetree. *Magn Reson Med*. 2015; doi: 10.1002/mrm.25640
24. Balu N, Yarnykh VL, Chu B, et al. Carotid plaque assessment using fast 3D isotropic resolution black-blood MRI. *Magn Reson Med*. 2011; 65:627–637. [PubMed: 20941742]
25. Lindley, MD., Kim, D., Morrell, G., et al. High-permittivity thin dielectric pad improves peripheral non-contrast MRA at 3T. Milan: ISMRM; 2014. 2014
26. Webb AG. Dielectric materials in magnetic resonance. *Concepts Magn Reson Part A*. 2011; 38:148–184.
27. Corti R, Osende JI, Fayad ZA, et al. In vivo noninvasive detection and age definition of arterial thrombus by MRI. *J Am Coll Cardiol*. 2002; 39:1366–1373. [PubMed: 11955857]
28. Pomposelli F. Arterial imaging in patients with lower extremity ischemia and diabetes mellitus. *J Vasc Surg*. 2010; 52(3 Suppl):81S–91S. [PubMed: 20804938]
29. Ohtake T, Oka M, Ikee R, et al. Impact of lower limbs' arterial calcification on the prevalence and severity of PAD in patients on hemodialysis. *J Vasc Surg*. 2011; 53:676–683. [PubMed: 21211928]
30. Liabeuf S, Olivier B, Vemeer C, et al. Vascular calcification in patients with type 2 diabetes: the involvement of matrix Gla protein. *Cardiovasc Diabetol*. 2014; 13:85. [PubMed: 24762216]
31. Balu, N., Wang, J., Zhao, X., et al. Targeted multi-contrast vessel-wall imaging of bilateral peripheral artery disease. Proceedings of the 18th Annual Meeting of ISMRM; Stockholm, Sweden. 2010. p. 3685
32. Edelman RR, Flanagan O, Grodzki D, et al. Projection MR imaging of peripheral arterial calcifications. *Magn Reson Med*. 2015; 73:1939–1945. [PubMed: 24957402]
33. Grodzki DM, Jakob PM, Heismann B. Ultrashort echo time imaging using pointwise encoding time reduction with radial acquisition (PETRA). *Magn Reson Med*. 2012; 67:510–518. [PubMed: 21721039]
34. Fayad ZA. MR imaging for the noninvasive assessment of atherothrombotic plaques. *Magn Reson Imaging Clin N Am*. 2003; 11:101–113. [PubMed: 12797513]
35. Underhill HR, Hatsukami TS, Fayad ZA, et al. MRI of carotid atherosclerosis: clinical implications and future directions. *Nat Rev Cardiol*. 2010; 7:165–173. [PubMed: 20101259]
36. Chi J, Chiu B, Cao Y, et al. Assessment of femoral artery atherosclerosis at the adductor canal using 3D black-blood MRI. *Clin Radiol*. 2013; 68:e213–e221. [PubMed: 23332436]
37. Isbell DC, Meyer CH, Rogers WJ, et al. Reproducibility and reliability of atherosclerotic plaque volume measurements in peripheral arterial disease with cardiovascular magnetic resonance. *J Cardiovasc Magn Reson*. 2007; 9:71–76. [PubMed: 17178683]
38. Naghavi M, Libby P, Falk E, et al. From vulnerable plaque to vulnerable patient: a call for new definitions and risk assessment strategies: part II. *Circulation*. 2003; 108:1772–1778. [PubMed: 14557340]
39. Saam T, Hatsukami TS, Takaya N, et al. The vulnerable, or high-risk, atherosclerotic plaque: noninvasive MR imaging for characterization and assessment. *Radiology*. 2007; 244:64–77. [PubMed: 17581895]
40. Polonsky TS, Liu K, Tian L, et al. High-risk plaque in the superficial femoral artery of people with peripheral artery disease: prevalence and associated clinical characteristics. *Atherosclerosis*. 2014; 237:169–176. [PubMed: 25240112]
41. Okura H, Asawa K, Kubo T, et al. Incidence and predictors of plaque rupture in the peripheral arteries. *Circ Cardiovasc Interv*. 2010; 3:63–70. [PubMed: 20160185]

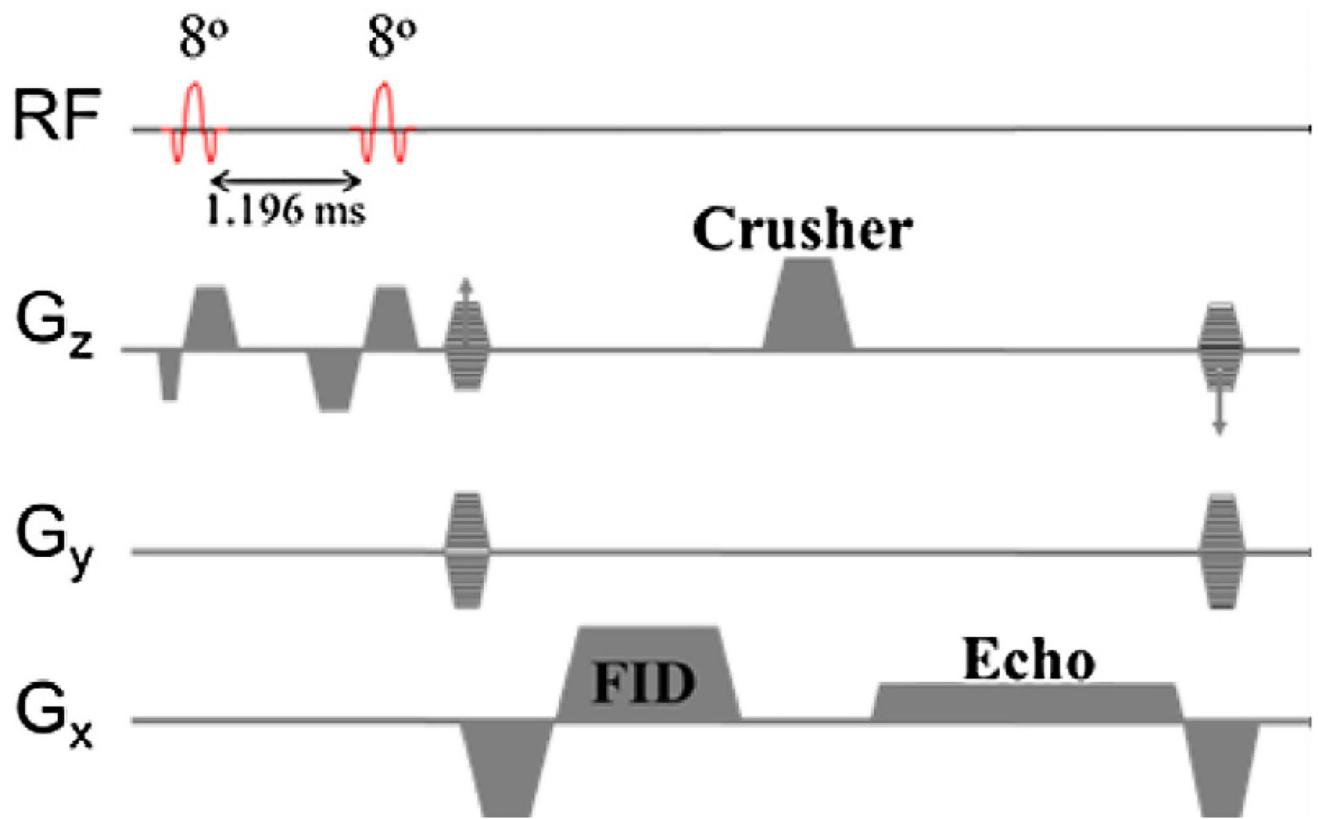


Figure 1. Water-selective three-dimensional double-echo steady-state pulse sequence. The free induction decay is read out with higher bandwidth to minimize TR and increase muscle tissue SNR of echo. Interpulse time is computed based on the chemical shift value of lipid CH_2 protons at 2.89 T (-418 Hz relative to H_2O). G_x , Gradient pulses in x-axis; G_y , Gradient pulses in y-axis; G_z , Gradient pulses in z-axis. (Color version of figure is available online).

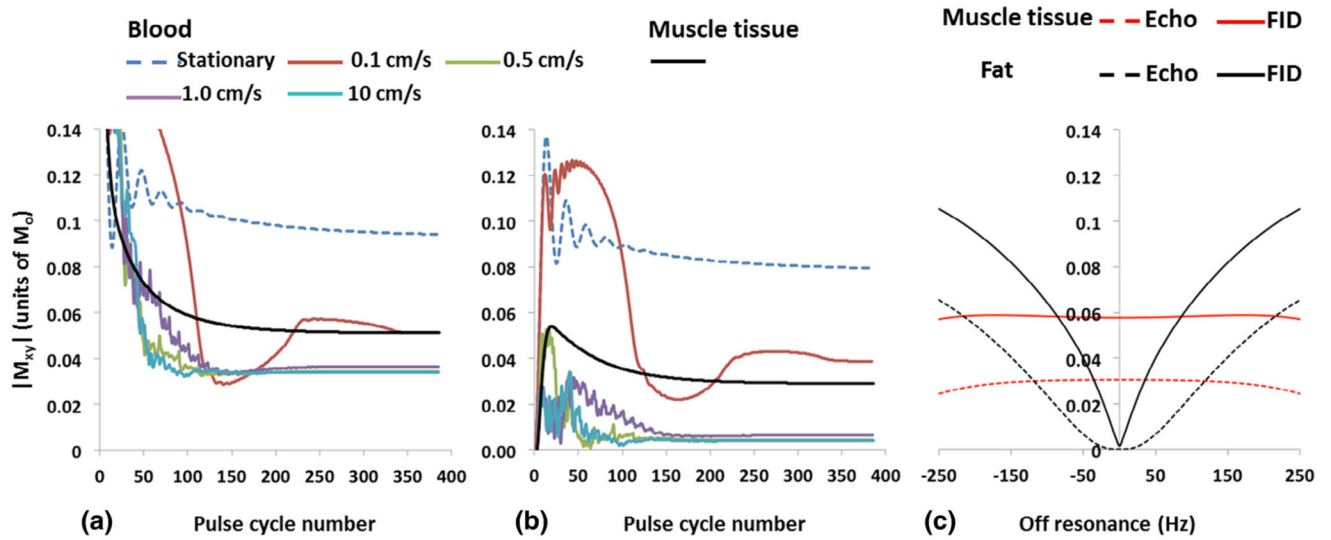


Figure 2.

Flow sensitivity and off-resonance effects of 1–1 binomial pulse. Simulation of steady-state signal under different flow condition for **(a)** SSFP-free induction decay (FID) and **(b)** SSFP-Echo. Significant SSFP-Echo signal attenuation even at low velocity of 0.5 cm/s supports excellent blood suppression observed even near the walls of peripheral veins, e.g. Figure 3b and f. **(c)** FID as a gradient-recalled echo is much less tolerant of static field inhomogeneity. The simulation suggests that it is possible to discern intermuscular fat from vessel wall up to 100 Hz off-resonance. (Color version of figure is available online).

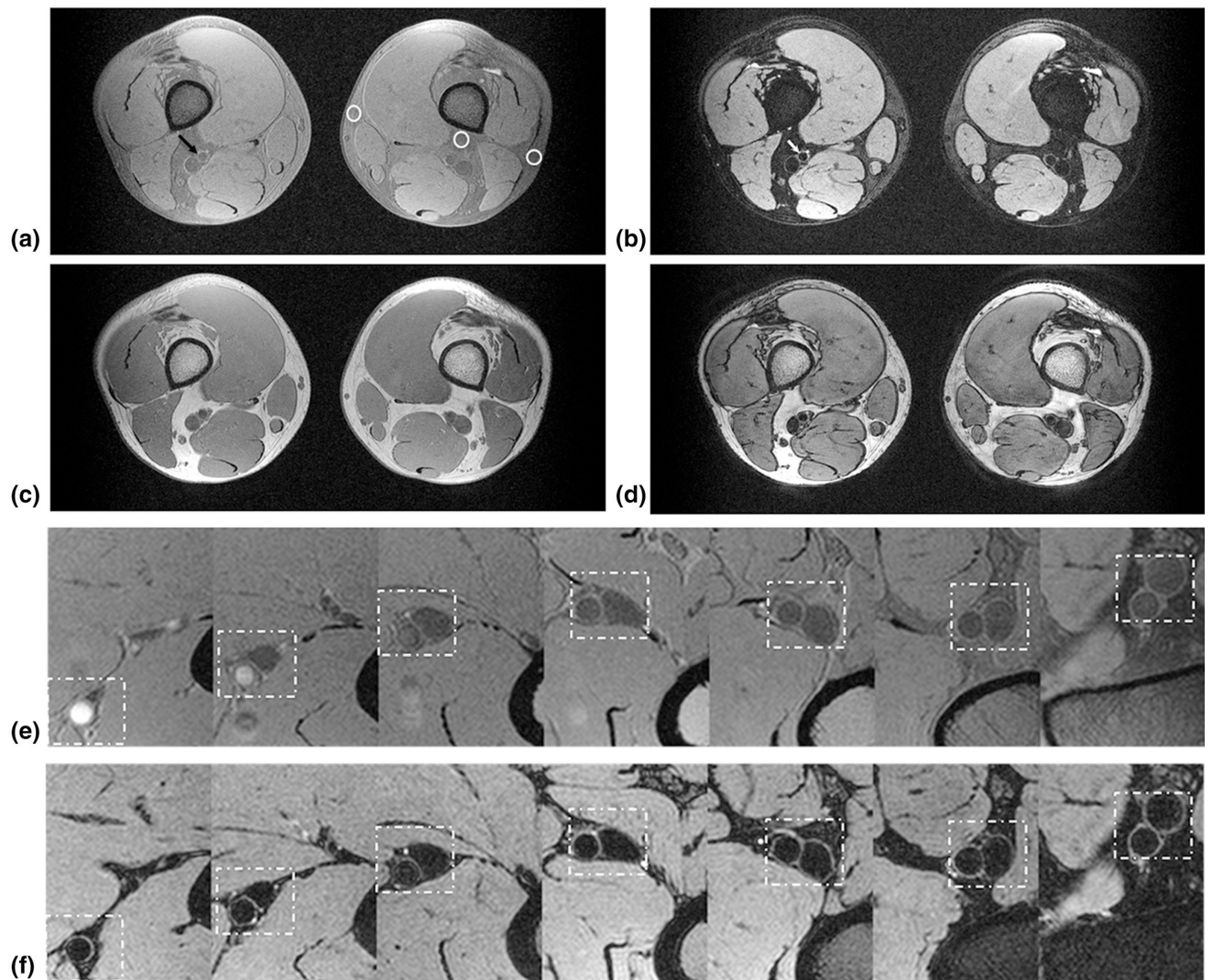


Figure 3. Dual lumen contrast of DESS images. The images of (a) SSFP-free induction decay (FID), and (b) SSFP-Echo, clearly demonstrate distinct lumen contrast in the superficial femoral artery, i.e. moderate (gray blood [GB], *black arrow*) signal in the lumen (a) versus full suppression (black blood [BB], *white arrow*) of the blood signal (b). *White circles* highlight variation of fat attenuation due to spatially dependent static field inhomogeneity. From left to right, the fat signal reduction is 54%, 67%, and 75%, respectively, compared to the (c) GB image acquired without fat attenuation. At the same ROIs in (b) the fat signal reduction is 70%, 88%, and 92% compared to (d), collected simultaneously with (c). Magnified view of femoral and popliteal arteries (*dashed box*) of (e) SSFP-FID and (f) SSFP-Echo from proximal to the distal edge of the slab (seven slices out of 240, each separated by 45 mm). The signal in (e) is strongly location dependent, being highest in the most proximal location due to inflow enhancement, getting gradually lower in the more distal slices.

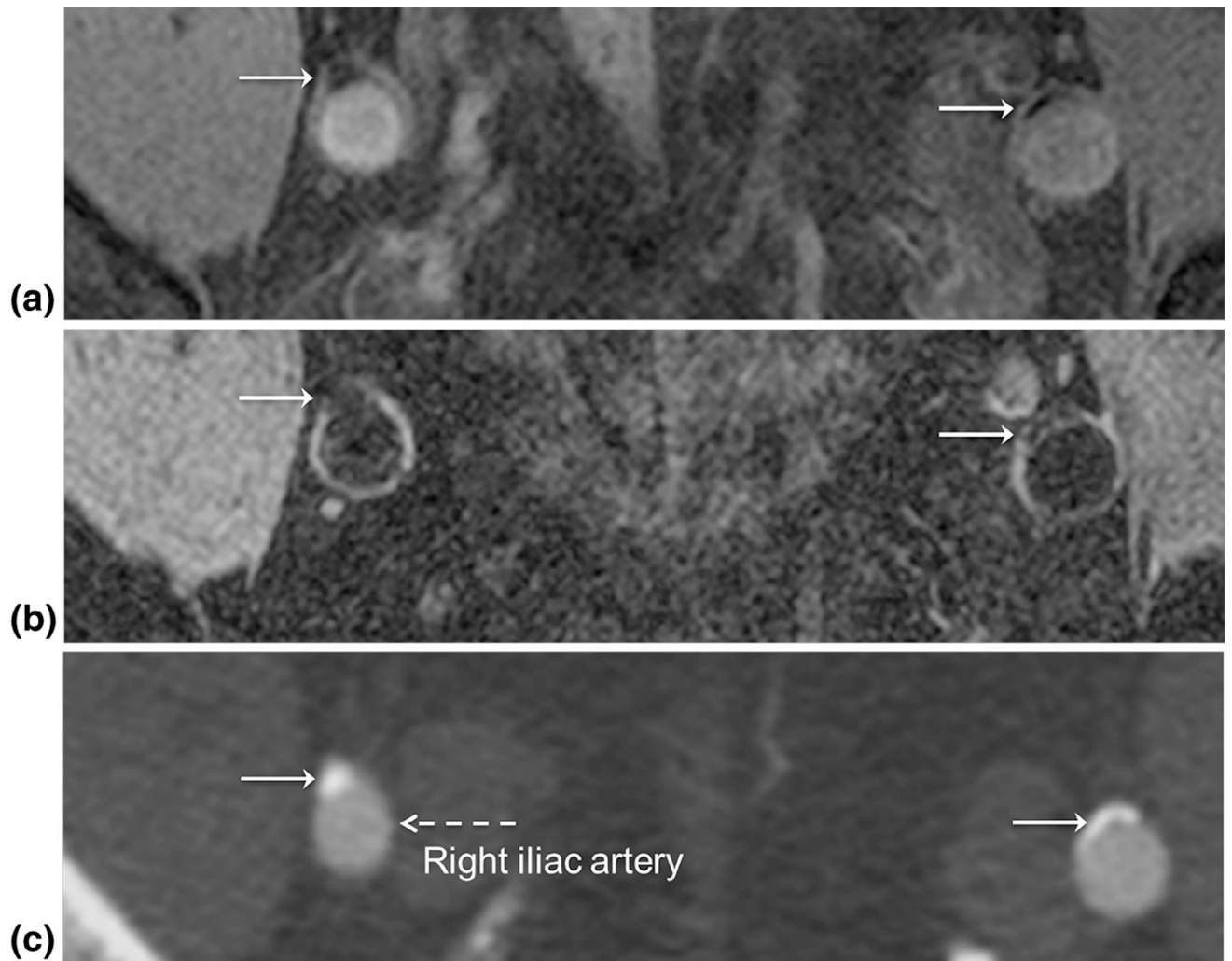


Figure 4. Identification of calcium in peripheral artery disease using double-echo steady state. On both (a) gray blood and (b) black blood images calcium (*white arrows*) is hypointense with distinct lumen contrast allowing detection of calcium. (c) Proof of calcium (*white arrows*) in iliac arteries on computed tomography angiography. The lumen (*dashed arrow*) is also well visualized from the contrast medium that has a higher radiodensity than surrounding tissue. The patient is a 71-year-old female with ankle-brachial index (ABI) = 0.77 and 0.58 in left and right leg, respectively.

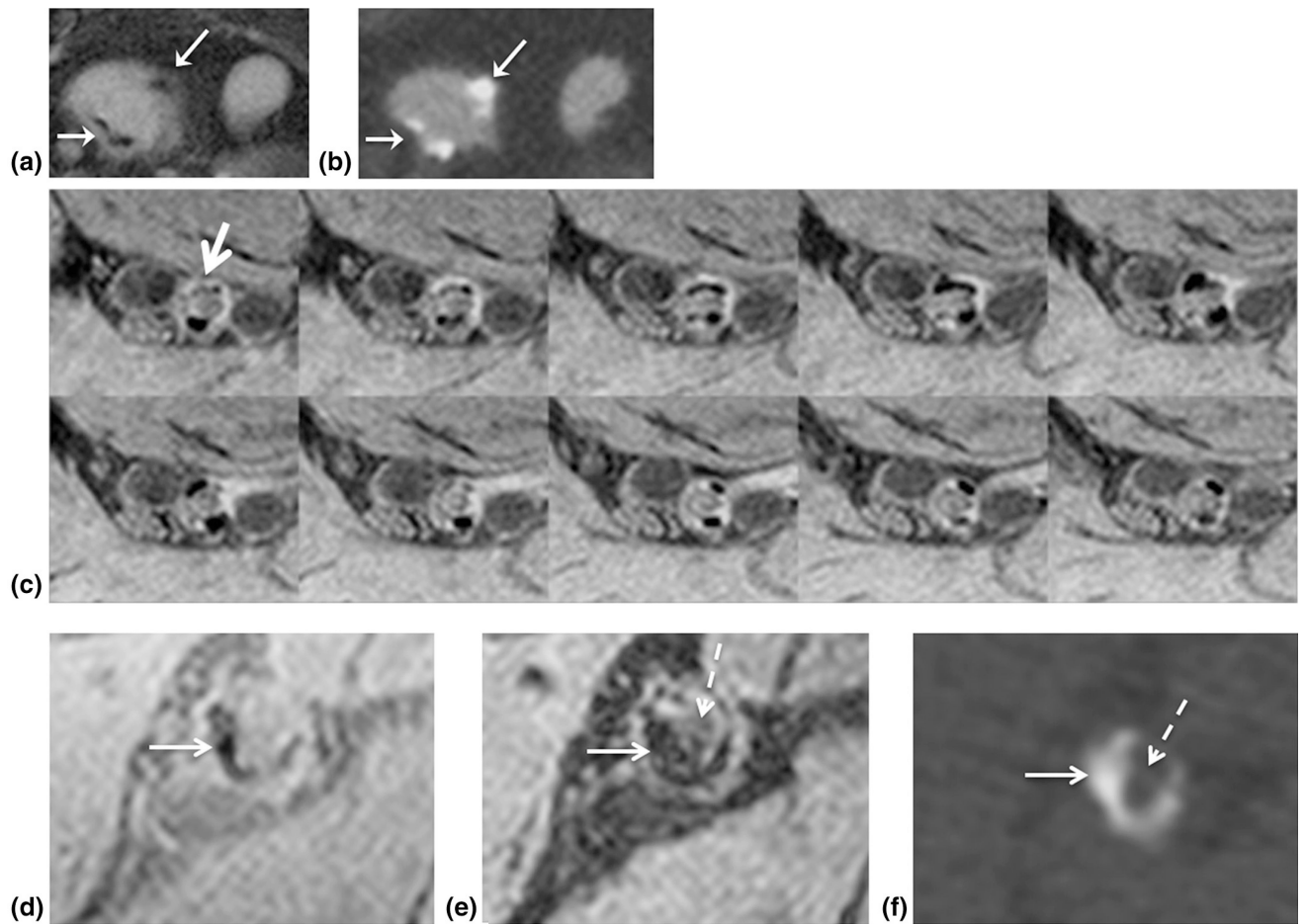


Figure 5.

Detection of calcium. Visualization of calcium (*arrows*) in right common iliac artery aneurysm on (a) gray blood (GB) and (b) computed tomography angiography (CTA) images (same patient as in Fig 4). (c) Magnified view of 10 contiguous slices representing 1.5 cm of the right tibial-peroneal arterial segment (*arrow*) in a 66-year-old type-2 diabetic patient with ABI = 0.57. Spatially registered (d) GB and (e) black blood images corroborate calcium (*white arrow*) and obstruction (*dashed arrow*) in (e) detected by (f) CTA in left superficial femoral artery (SFA). Hypointense lumen signal (*dashed arrow*) surrounded by calcium (*white arrow*) in right superficial femoral arteries indicates obstruction.

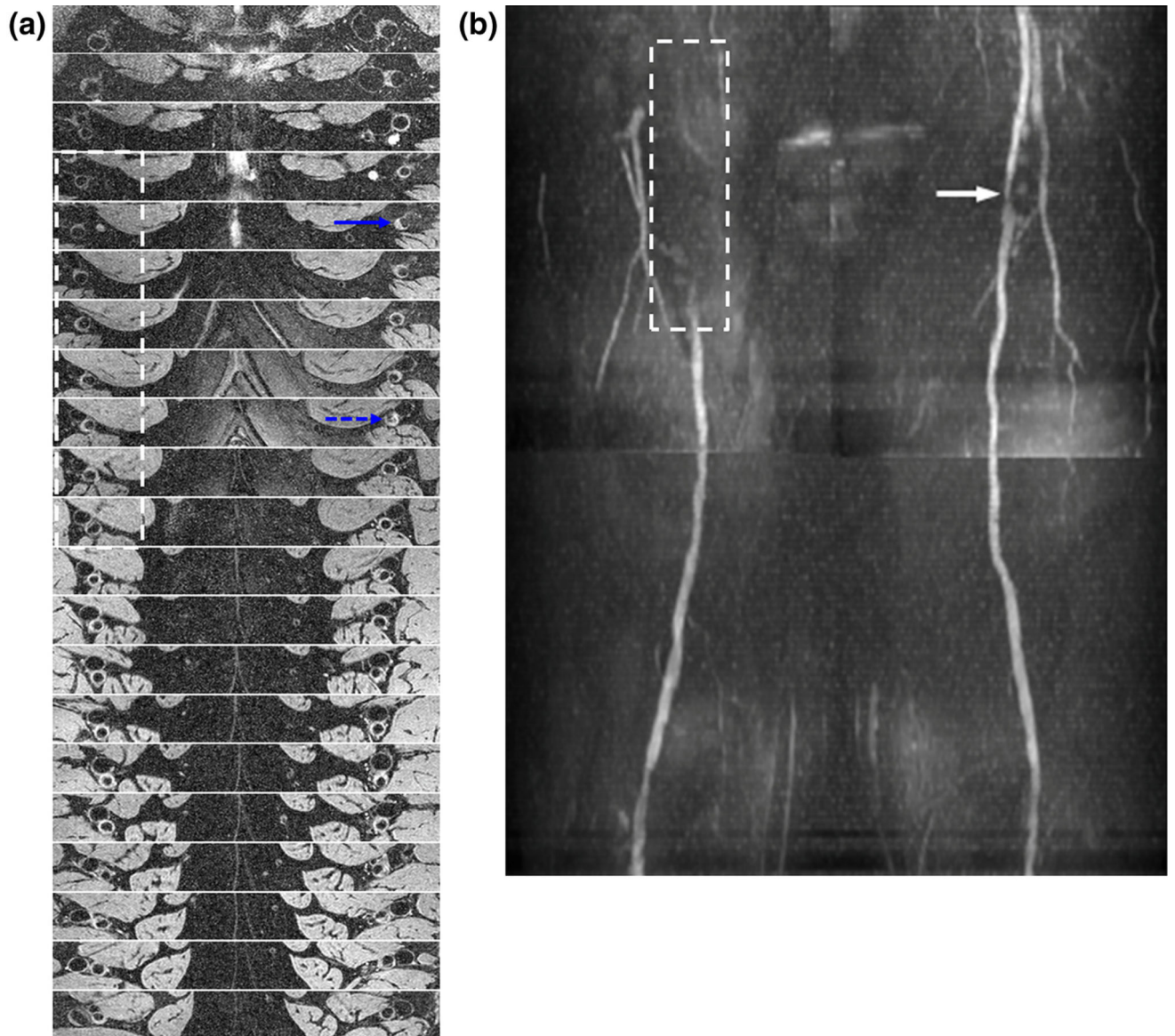


Figure 6.

Unambiguous assessment of lesion burden with black-blood images in a 51-year-old male with ABI = 0.83 (left) and 0.9 (right): **(a)** 20 slices spanning 300 mm cranio-caudally from the common femoral artery (CFA) to distal superficial femoral arteries (SFA); slice spacing 15 mm. **(b)** The luminal narrowing seen on the quiescent interval single-shot magnetic resonance angiography (*white arrow*) is consistent with the axial images of **(a)** (*blue dashed arrow*). The *dashed box* indicates the commonly observed B₁ inhomogeneity-induced signal loss in the right proximal femoral artery at 3T. The signal attenuation is also observed in **(a)** but is less pronounced (*dashed box*) such that the visualization of the lesion burden and eccentricity is still possible. *Solid blue arrow* points to an eccentric lesion. (Color version of figure is available online).

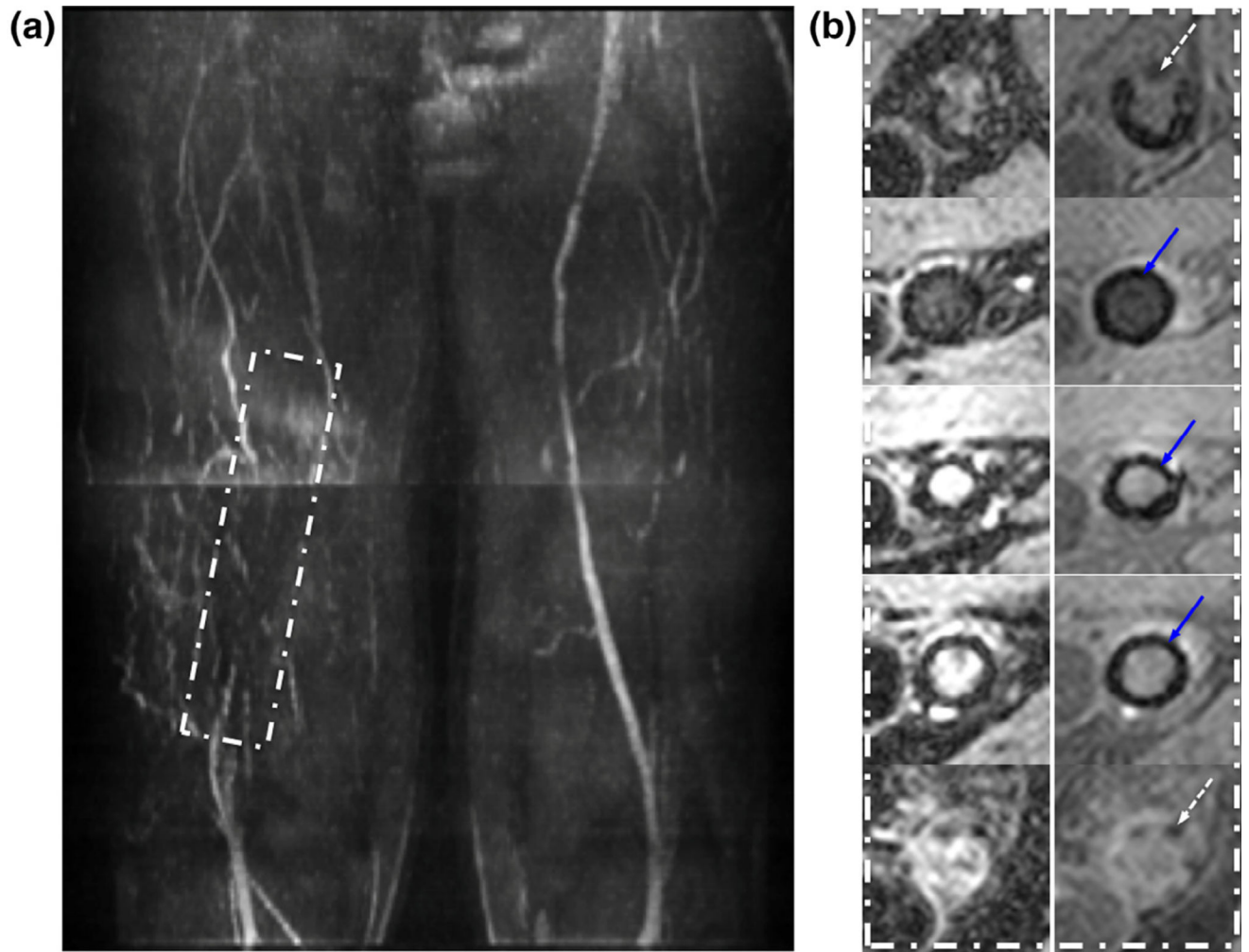


Figure 7.

In-stent restenosis in a 57-year-old male with ABI = 0.51 (right) and 0.93 (left): **(a)** MIP in the anterior–posterior direction of quiescent interval single-shot magnetic resonance angiography with stent in medial to distal superficial femoral arteries (*rectangle*). **(b)** Select black blood (left column, signal void imply stent patency) and gray blood (right column) images showing in-stent restenosis. *Top and bottom rows* show end rungs of stent (signal voids distributed symmetrically around the circumference, *dashed arrow*). In the middle, three rows signal void (*blue arrows*) near the vessel wall are attributed to the stent rather than calcification. (Color version of figure is available online).

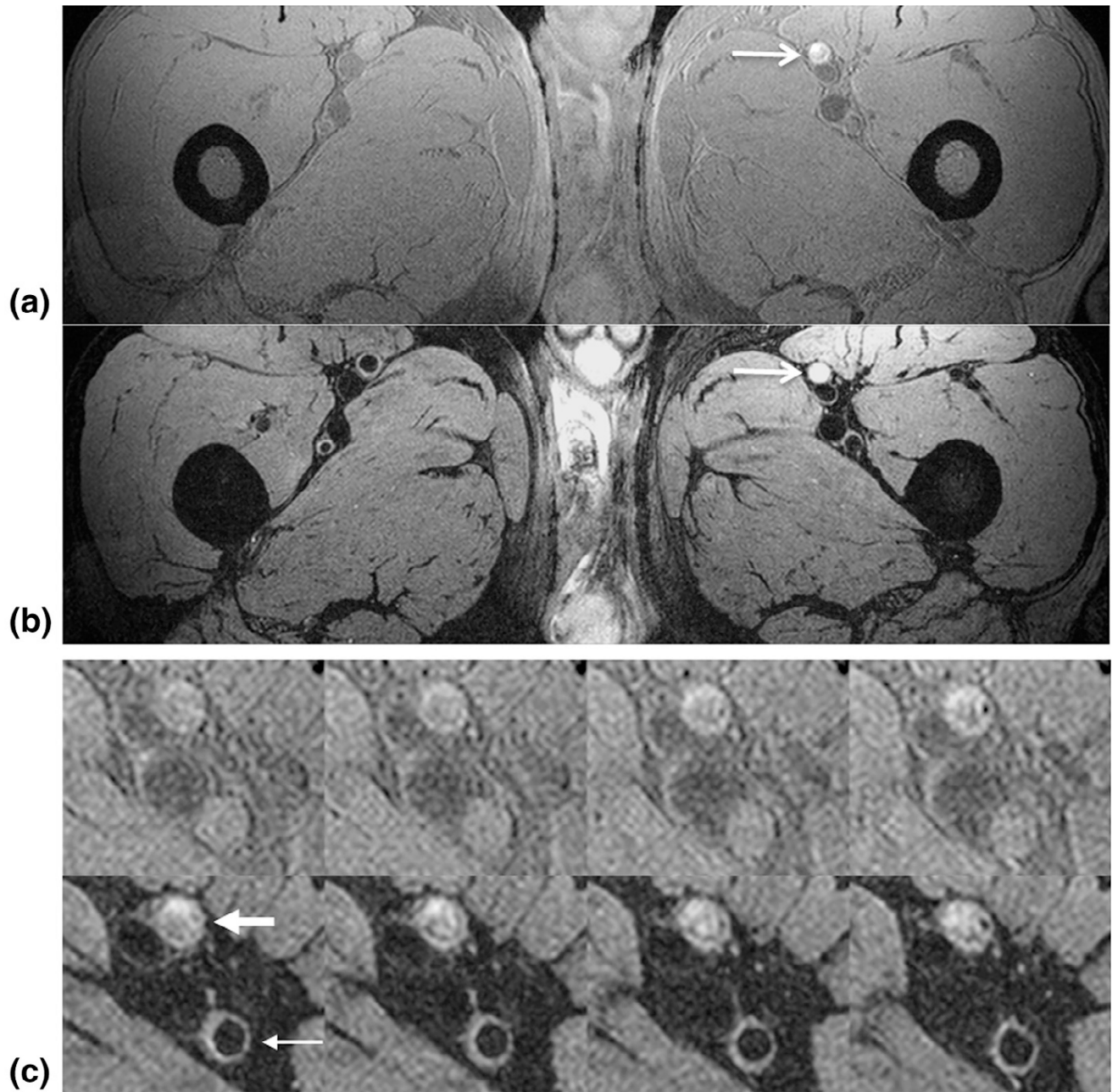


Figure 8.

Arterial thrombus in a 63-year-old patient with peripheral artery disease with ABI = 0.73 and 1.04 in left and right leg, respectively. Hyperintense signal of left superficial femoral arteries lumen (*arrows*) on both (a) gray blood (GB) and (b) black blood (BB) image suggests a newly formed arterial thrombus. (c) GB (*top row*) and BB images of superficial (*thick arrow*) and deep (*thin arrow*) femoral arteries 8.9 cm distal from the common femoral artery bifurcation. The reduced signal level relative to the adjacent muscle tissue as compared to (a) indicates that the thrombus is several weeks old.

TABLE 1

SNR and CNR Measured from Black-blood Images

Subject	Lumen and Vessel-wall SNR and CNR* (SNR _l /SNR _w)		
	Common Fem.	Superficial Fem.	Popliteal
1	4.7/15.4	5.0/23.7	7.3/27.3
2	8.5/15.4	9.5/30.8	6.0/20.1
3	10.9/19	11.7/36.7	8.6/31.8
4	8.5/20.1	10.1/27.3	8.8/29.6
5	5.7/13.0	6.9/17.8	5.6/21.3
6	10.7/34.4	15.4/39.1	13.0/55.7
7	5.8/16.6	6.3/23.7	8.1/17.8
8	5.5/17.8	7.3/28.4	6.8/19.0
9	7.9/15.4	7.1/35.5	6.6/24.9
10	6.6/17.8	6.3/21.3	5.1/13.0
11	7.7/28.4	7.9/37.9	7.2/27.3
12	6.4/19.0	6.9/22.5	6.9/27.3
13	8.9/17.8	7.5/23.7	8.5/37.9
14	8.6/21.3	8.3/28.4	8.2/23.7
15	10.5/29.6	8.6/23.7	9.5/33.2
16	9.1/23.7	9.4/30.8	9.5/36.7
17	6.6/14.2	7.1/21.3	6.3/36.7
18	11.3/34.4	8.5/16.6	9.5/32.0
19	11.8/32.0	13.0/35.5	9.7/32.0
20	10.4/26.1	9.5/29.6	8.9/29.6
Average			
SNR _w (SD)/SNR _l (SD)	8.3 (2.2)/21.6 (6.9)	8.6 (2.5)/27.7 (6.7)	8.0 (1.8)/28.8 (9.3)
Average:			
CNR (SD)	13.2 (5.4)	19.1 (5.4)	20.8 (7.9)

SNR_w, SNR of vessel-wall; SNR_l, SNR of vessel lumen; SD, standard deviation; Fem., femoral.

* CNR between the wall and lumen is defined as SNR_w-SNR_l.

TABLE 2

SNR and CNR Measured from Gray-blood Images

Subject	Lumen and Vessel-wall SNR and CNR* (SNR _l /SNR _w)		
	Common Fem.	Superficial Fem.	Popliteal
1	51.3/38.0	50.7/39.3	22.0/32.0
2	16.7/19.3	20.0/28.7	15.3/24.0
3	38.0/26.7	34.0/55.3	32.0/44.7
4	50.0/32.7	28.0/34.7	30.0/44.0
5	24.7/27.3	25.3/29.3	20.0/28.0
6	57.9/46.7	59.6/45.8	24.2/33.3
7	29.3/21.3	33.3/38.0	16.0/22.0
8	21.3/22.0	53.3/42.7	26.0/29.3
9	37.3/33.3	44.0/44.0	26.7/34.0
10	30.7/20.0	19.3/32.0	21.3/29.3
11	32.7/41.3	35.3/41.3	33.3/44.0
12	54.0/28.7	51.3/40.0	26.7/36.0
13	68.0/46.0	37.3/32.0	35.3/50.5
14	48.0/45.3	18.7/28.7	16.0/26.7
15	36.0/32.7	15.3/28.0	20.0/34.7
16	47.3/45.3	42.7/42.7	28.7/40.7
17	16.7/21.3	15.3/26.7	21.3/38.0
18	30.7/45.3	53.3/52.7	34.7/38.0
19	21.3/30.0	35.3/38.7	50.0/45.3
20	22.0/28.0	16.7/28.0	36.7/42.7
Average			
SNR _w (SD)/SNR _l (SD)	32.6 (9.7)/36.7 (14.8)	37.4 (8.4)/34.4 (14.4)	35.8 (7.8)/26.8 (8.6)
Average:			
CNR (SD)	-4.1 (10.7)	3.0 (9.6)	9.0 (4.9)

SNR_w, SNR of vessel-wall; SNR_l, SNR of vessel lumen; SD, standard deviation; Fem., femoral.

* CNR between the wall and lumen is defined as SNR_w-SNR_l.